




## Article

# Fluid inclusions in amethyst quartz of different geological environments from Brazil

Coralie Heinis Dias<sup>1\*</sup> , Mario Luiz de Sá Carneiro Chaves<sup>2</sup>, Rosaline Cristina Figueiredo e Silva<sup>2</sup>  
and Sylvio Dutra Gomes<sup>3</sup>

<sup>1</sup>Universidade do Estado de Minas Gerais, Departamento de Geociências, Ciências Humanas e Linguagens, Av. Brasília, 1304, Bairro Baú, João Monlevade, Minas Gerais, 35930-314, Brazil; <sup>2</sup>Universidade Federal de Minas Gerais, Departamento de Geologia, Av. Antônio Carlos, 6627, Belo Horizonte, Minas Gerais, 31270-901, Brazil; and <sup>3</sup>Universidade Federal da Bahia, Instituto de Geociências, R. Barão de Jeremoabo, s/n, Ondina, Salvador, Bahia, 40170-290, Brazil.

### Abstract

Fluid-inclusion studies were conducted on amethyst quartz from three different geological environments: basalt cavities; hydrothermal veins; and granitic pegmatites of Eastern Brazil, to understand the conditions of amethyst crystallisation in each of these environments. In samples from basalt cavities, fluid inclusions are exclusively one-phase aqueous types suggesting a low-temperature formation environment. Crystals from the two other environments show that fluid inclusions can be either one-phase aqueous, two-phase aqueous, three-phase aqueous carbonic, or three-phase aqueous with the presence of precipitated solid halite. The carbonic composition of the system H<sub>2</sub>O–CO<sub>2</sub>–NaCl was confirmed by Raman spectroscopic analysis and suggests a metamorphic or magmatic fluid source. Fluid inclusions trapped in samples from hydrothermal veins reveal at least two different fluid generations based on homogenisation temperatures. The first generation has minimum trapping temperatures between 249°C and 391°C. The second generation of lower temperature fluids has minimum trapping temperatures varying from 82°C to 203°C. Fluid inclusions of this group record eutectic temperatures that indicate the presence of Ca and Fe cations in addition to Na. Fluid inclusions trapped in amethyst from a pegmatite body have moderate salinity values between 15 and 25 eq. wt.% NaCl, thus reflecting the elevated salt content in pegmatite-forming fluids. In this sample, the first fluid generation is represented by aqueous fluid inclusions with minimum trapping temperatures ranging from 268°C to 375°C. The estimated eutectic temperatures, generally below –50°C, indicate the presence of Ca cations in addition to Na. Minimum trapping temperatures correspond to temperatures of late-to-post-pegmatitic hydrothermal stages. The second generation records minimum trapping temperatures between 125°C and 247°C. Amethyst from both hydrothermal veins and pegmatite environments contain solid inclusions of hematite, an indication that the mineralising fluid was Fe rich and thus, possibly magmatic in origin.

**Keywords:** fluid inclusions, amethyst, basalt, hydrothermal vein, pegmatite

(Received 17 September 2020; accepted 12 April 2021; Accepted Manuscript published online: 19 April 2021; Associate Editor: Daniel Atencio)

### Introduction

Amethyst, the violet variety of quartz, is a gemmological material that can be found in different geological environments. In Minas Gerais State, Brazil (Fig. 1), amethyst quartz deposits primarily occur: filling cavities in basaltic rocks (geodes) of the Triângulo Mineiro area; in hydrothermal veins associated with the geological units of the Espinhaço mountain range; and in granitic pegmatites from the Eastern Brazilian Pegmatite Province.

A summary of the main environments of worldwide amethyst formation, their temperature ranges and types of fluids involved is given by Gilg (2012). According to Gilg, amethyst can be formed in: miarolitic cavities of intrusive felsic rocks, at temperatures up to 300°C by gas-rich magmatic brines; in epithermal veins in felsic-to-intermediate volcanic terrains at temperatures between

160°C and 270°C, by low-salinity meteoric fluids; in low-temperature veins in gneiss, granite and ferruginous quartzite at temperatures below 150°C by fluids of variable salinity with low gas content; and in geodes hosted in basaltic volcanic rocks, by low-salinity connate fluids with low gas contents at maximum temperatures of 100°C.

Gilg *et al.* (2003) and Commin-Fischer *et al.* (2010) reported maximum trapping temperatures of 100°C and low-salinity fluids for amethyst hosted in basalt cavities at Rio Grande do Sul, Brazil. For amethyst related to Cretaceous granite in South Korea, Yang *et al.* (2001) discussed higher formation temperatures, between 280°C and 400°C, and average salinity of 4 eq. wt.% NaCl. Dumanska-Slowik *et al.* (2017) studied fluid inclusions trapped in amethyst associated with Lower Cambrian siltstone–sandstone, and report homogenisation temperatures between 210°C and 330°C and salinity values between 6 and 13 eq. wt.% NaCl. According to those authors, amethyst is formed by fluids hotter than for colourless quartz, which record homogenisation temperatures between 154°C and 219°C. This present work focuses on petrographic and microthermometric studies of fluid inclusions

\*Author for correspondence: Coralie Heinis Dias, Email: [coralie.dias@uemg.br](mailto:coralie.dias@uemg.br)

Cite this article: Heinis Dias C., de Sá Carneiro Chaves M.L., Figueiredo e Silva R.C. and Dutra Gomes S. (2021) Fluid inclusions in amethyst quartz of different geological environments from Brazil. *Mineralogical Magazine* 85, 332–347. <https://doi.org/10.1180/mgm.2021.38>

**Table 1.** Location information for the three environments sampled.

Genetic environment	Volcanic	Metamorphic-hydrothermal	Pegmatite
Mineralisation type	Geodes and cavities	Quartz veins with amethyst	Amethyst aggregates on milky quartz
Location name	Barreiro Farm	Sobrado Farm	Itajobi Farm
County/State	Tupaciguara/Minas Gerais	Felício dos Santos/Minas Gerais	Pancas/Espírito Santo
UTM latitude	7951970N	7997949N	7870342N
UTM longitude	708060E	692039E	306017E
UTM zone	23K	23K	24K
Host rock	Weathered basalt	Mica-quartz schist	Weathered pegmatite

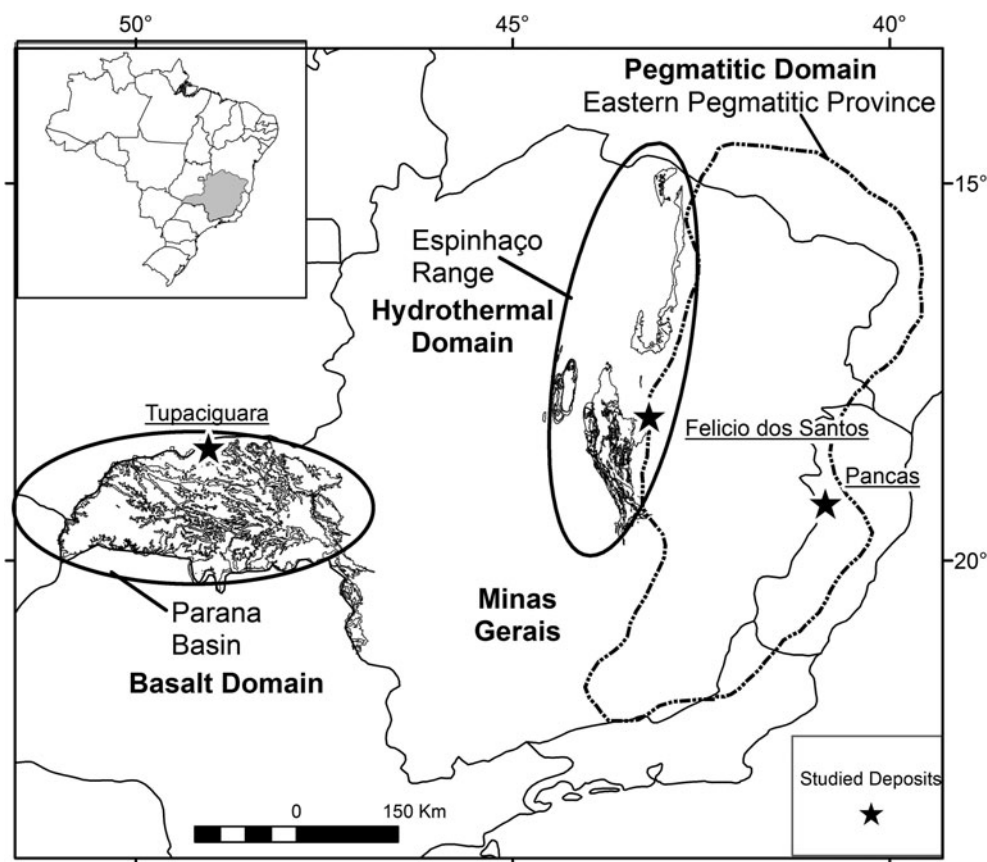


**Fig. 1.** Map of Minas Gerais State indicating the sample locations (black star): Tupaciguara (amethyst from basaltic rocks), Felício dos Santos (amethyst from metamorphic quartz veins); and Pancas (amethyst from granitic pegmatite). The basalt, hydrothermal and pegmatitic domains are shown. Based on Pinto and Silva (2014).

trapped in amethyst quartz from the three main genetic environments in Brazil, to better understand the conditions of crystallisation. The main techniques used are freezing and heating of fluid inclusions and Raman spectroscopy. We also attempt to distinguish amethyst types on the basis of their genesis and fluid composition.

### Materials and methods

The samples selected are predominantly amethyst quartz from three distinct geological environments in the state of Minas Gerais (MG) and surrounding regions (Fig. 1; Table 1): cavities in basaltic rocks from the Serra Geral Formation, Tupaciguara municipality, in the Triângulo Mineiro area (MG) (Fig. 2a); metamorphic veins in metasedimentary rocks from the Macaúbas Group, Felício dos Santos municipality (MG) (Fig. 2b); and

granitic pegmatite from the Eastern Brazilian Pegmatite Province, Pancas municipality, in the state of Espírito Santo (Fig. 3). Four doubly polished thin sections, cut parallel to the 'c' axis, were prepared to study the fluid inclusions in single crystals or amethyst crystal aggregates (Figs 2, 3). Thin sections were labelled T1 (amethyst crystal from Tupaciguara), FS1 (amethyst crystal from Felício dos Santos), FS2 (second amethyst crystal from Felício dos Santos) and P1 (amethyst crystal aggregate from Pancas).

Inclusions were mapped initially using a Leica optical microscope with an integrated Leica DFC290 camera, at the Manoel Teixeira da Costa Research Center/CPMTC-IGC-UFGM Metallogeny Laboratory, in order to locate, describe, classify and group the inclusions in assemblages (fluid-inclusion assemblages – FIA) according to Goldstein and Reynolds (1994) criteria. FIAs were classified as primary, pseudo-secondary or secondary based on Shepherd *et al.*

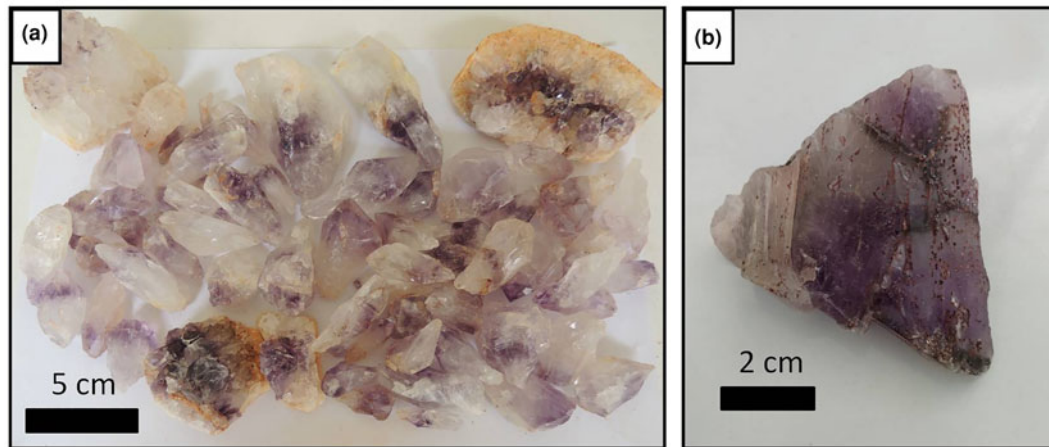


**Fig. 2.** Selected amethyst samples: (a) crystals from a basalt cavity in the Tupaciguara deposit; and (b) sample from a hydrothermal vein in the Felício dos Santos deposit.

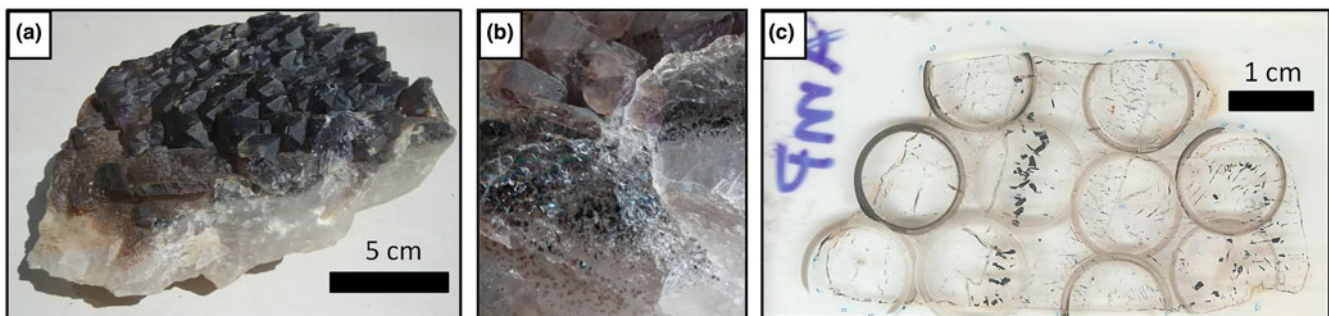


**Fig. 3.** (a) Amethyst crystal aggregate from a pegmatite (Pancas county); (b) detail of hematite solid inclusions in the same sample; and (c) thin section from this sample after making the cuts with a cutting wheel, delimiting the regions selected in the mapping stage.

(1985) and Bodnar (2003). The selected regions were marked on the thin sections and removed using a cutting wheel (Fig. 3c), at the UFMG Microscopy Center, followed by immersion in acetone to remove the coverslip. Each piece (chip) was named C1, C2, C3..., and the assemblages measured on each chip C1FIA1, C1FIA2, etc.

The microthermometric studies were conducted on an automated Linkam THMSG600 heating/freezing stage with a temperature controller TMS93 coupled to a Leica petrographic microscope, at the CPMTIC Metallogeny Laboratory, using *Linksys 32* software to control and record the experiments. Freezing and heating experiments were conducted on two- or three-phase fluid inclusions trapped in FS1, FS2 and P1 amethyst samples to obtain clathrate melting ( $T_{\text{clath}}$ ),  $\text{CO}_2$  melting ( $T_{\text{mCO}_2}$ ), first ice melting ( $T_e$ ), last ice melting ( $T_{\text{mIce}}$ ), hydrohalite melting ( $T_{\text{mHH}}$ ), halite final dissolution ( $T_{\text{mHal}}$ ) and total homogenisation temperatures (homogenisation temperature of the liquid and vapour phases –  $T_{\text{htot}}$ ). Homogenisation temperatures for aqueous carbonic inclusions were observed through the expansion of the  $\text{CO}_2$  phase, and for aqueous inclusions by homogenisation into a liquid phase.

The freezing tests reached  $-140^\circ\text{C}$ , and the heating tests  $\sim 500^\circ\text{C}$ . The stage was calibrated with synthetic  $\text{CO}_2$  and  $\text{H}_2\text{O}$  inclusions provided by Linkam. Measurement accuracy is  $\pm 0.1^\circ\text{C}$  for negative temperatures and  $\pm 1^\circ\text{C}$  for temperatures between  $0$ – $500^\circ\text{C}$ . The temperature measurements of clathrate melting ( $T_{\text{clath}}$ ), final ice melting ( $T_{\text{mIce}}$ ), hydrohalite melting ( $T_{\text{mHH}}$ ) and

total homogenisation (homogenisation temperature of liquid and vapour phases –  $T_{\text{htot}}$ ) obtained during the tests were entered into *MacFlincon* software (Brown and Hagemann, 1995) for density and salinity calculations. For the single halite final dissolution temperature acquired, salinity was obtained by the equations of Bowers and Helgeson (1983). The densities and salinities were calculated considering the equations for  $\text{H}_2\text{O}$ – $\text{CO}_2$ – $\text{NaCl}$  and  $\text{H}_2\text{O}$ – $\text{NaCl}$ – $[\text{KCl}]$  systems by Bowers and Helgeson (1983) and Bodnar and Vityk (1994), respectively.

In the absence of independent geothermometric data for the host rocks, it was not possible to calculate isochores and apply pressure corrections to homogenisation temperatures. As there is no evidence that satisfies the criteria for boiling (Ramboz *et al.*, 1982), the measured homogenisation temperatures are considered as the minimum trapping temperatures. Additional Raman spectroscopy analyses were taken at the Raman Spectroscopy Laboratory (Metallurgy Department of the Engineering School/UFMG), in order to support data interpretation from the microthermometric studies, as presented by Frezzotti *et al.* (2012). For Raman analysis a LabRam-HR 800 (Horiba Jobin Yvon) spectrograph was used, with a He–Ne laser (excitation at  $632.8\text{ nm}$ , focused to a spot of  $1$ – $2\ \mu\text{m}$ ), and an Olympus BX41 microscope provided with a long distance lens of  $\times 100$ . The collected back-scattered light was dispersed by a monochromator equipped with  $600\text{ gr/mm}$  grating and detected by a LN2 cooled CCD system. The spectra ranged from  $700$  to at least  $3700\text{ cm}^{-1}$  with a step

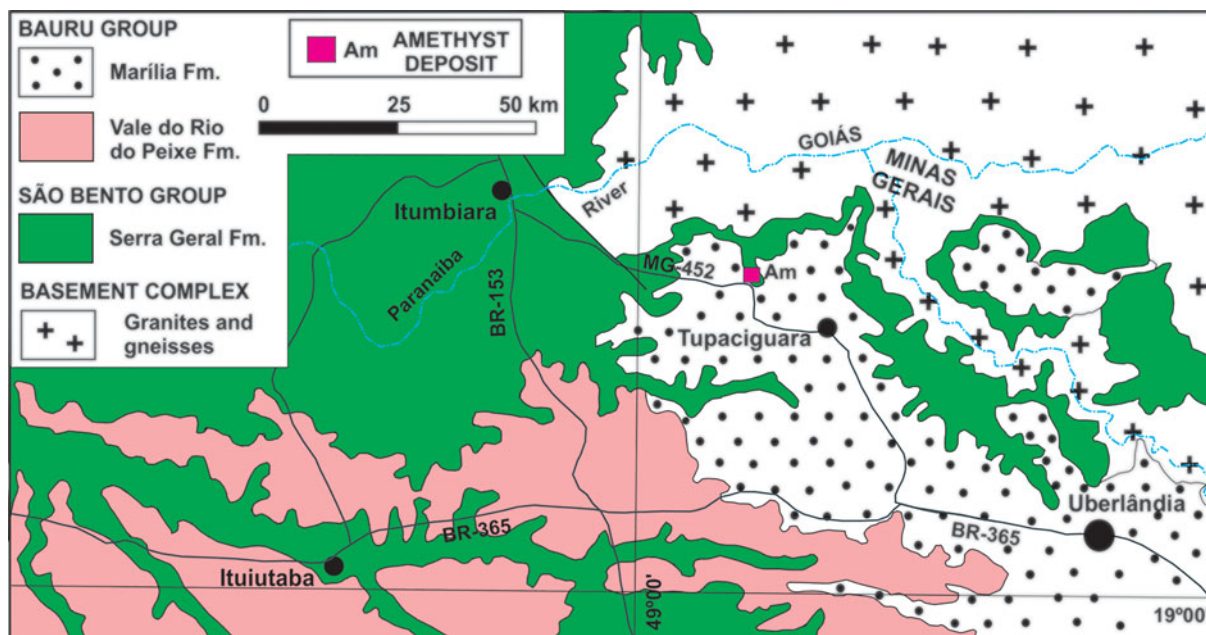


Fig. 4. Simplified geological context of Tupaciguara region. Based on Valente *et al.* (2004).

size of  $1.1 \text{ cm}^{-1}$ . The acquisition time ranged from 30 s to a maximum of one minute. To increase signal-to-noise ratio, spectra were acquired a minimum of ten times.

## Geological context

### Basalt cavity amethyst

Amethyst from basalt cavities occurs within the lava flows of the Paraná Basin, which can reach a thickness of 1700 m in an area of  $>900,000 \text{ km}^2$  in Brazil, Uruguay, Paraguay and Argentina (Piccirillo and Melfi, 1988; Frank *et al.*, 2009). In Minas Gerais, these flows occur exclusively in the Triângulo Mineiro region in the Serra Geral Formation (Fig. 4). In this type of mineralisation, amethyst occurs, in general, at the upper part of the central level of the lava flow, inside cavities that can also contain chalcedony, agate or hyaline quartz, in addition to zeolites, opal, calcite, gypsum and, more rarely, baryte (Juchem *et al.*, 1990; Juchem, 2013). The mineralised horizons are generally 1 to 5 m in thickness. The origin of the flows is related to the volcanic activity that occurred on the South American platform during the opening of the South Atlantic Ocean at ca. 135 Ma (Thiede and Vasconcelos, 2010; Dodd *et al.*, 2015). In the Tupaciguara region, the basement rocks crop out to the north and east, and consist of Neoproterozoic granites and gneisses. To the south, sedimentary rocks of the Upper Cretaceous Bauru Group occur.

The amethyst crystal selected originates from the Barreiro farm, Tupaciguara municipality, close to a highway (Table 1), where amethyst occurs in a regolith of weathered basalt (Fig. 5a). Crystals are found mainly in spherical to semi-spherical geodes, sometimes slightly elongated in one of the axes, and exhibit a centimetric-to-decimetric conical shape (Fig. 5b). The crystals are subhedral, have an elongated shape with a wider termination and show a light violet colour zoning, generally more intense from the centre to the apical portion of the crystal. Detailed petrography of the deposit host rocks is presented in

Dias *et al.* (2019) and described as a hypocrySTALLINE amygdaloidal basalt, with ophitic-to-subophitic texture. The main mineral assemblage is composed of plagioclase, clinopyroxene and glass, together with secondary iron oxides/hydroxides and smectite filling cavities or matrix interstices (Fig. 5c,d).

### Hydrothermal vein amethyst

Hydrothermal quartz veins are generally formed by devolatilisation reactions in rocks during regional metamorphism (Yardley, 1983), when quartz precipitates from silica-rich solutions as a result of decompression. In Minas Gerais State this type of deposit is the source of the majority of amethyst production. The amethyst samples from hydrothermal veins were collected at the Sobrado Farm deposit, also known as 'Lavra da Pedra Roxa' (Purple Stone mine), located  $\sim 7 \text{ km}$  southeast of Felício dos Santos municipality (Fig. 6). The deposit is located on the western flank of the Negra Range, to the east of Espinhaço mountains. There are numerous veins cutting the country rocks in the area, which are principally mica-quartz schists of the Neoproterozoic Capelinha Formation, Macaúbas Group (Tupinambá *et al.*, 1996). The formation of the veins is related to the regional deformation and metamorphism of the Araçuaí Orogeny between 630–480 Ma, in the Brasiliano cycle (Almeida, 1977; Pedrosa-Soares *et al.* 2011).

The Felício dos Santos amethyst mineralisation forms decametric-to-metric lenticular bodies commonly associated with kaolin. The host mica-quartz schist is extensively weathered (Fig. 7a). Crystals grow over colourless or milky quartz with hematite, with the upper end exhibiting a dark violet hue (Figs 2b,7b). According to Chaves and Coutinho (1992), the lenses are generally parallel to the host-rock foliation at  $\text{N}40^\circ\text{E}/20^\circ\text{NW}$ .

### Pegmatite amethyst

The pegmatite sample selected is from the Pancas municipality occurrence, in the state of Espírito Santo close to the border with Minas Gerais (Fig. 8). It is commonly difficult to certify

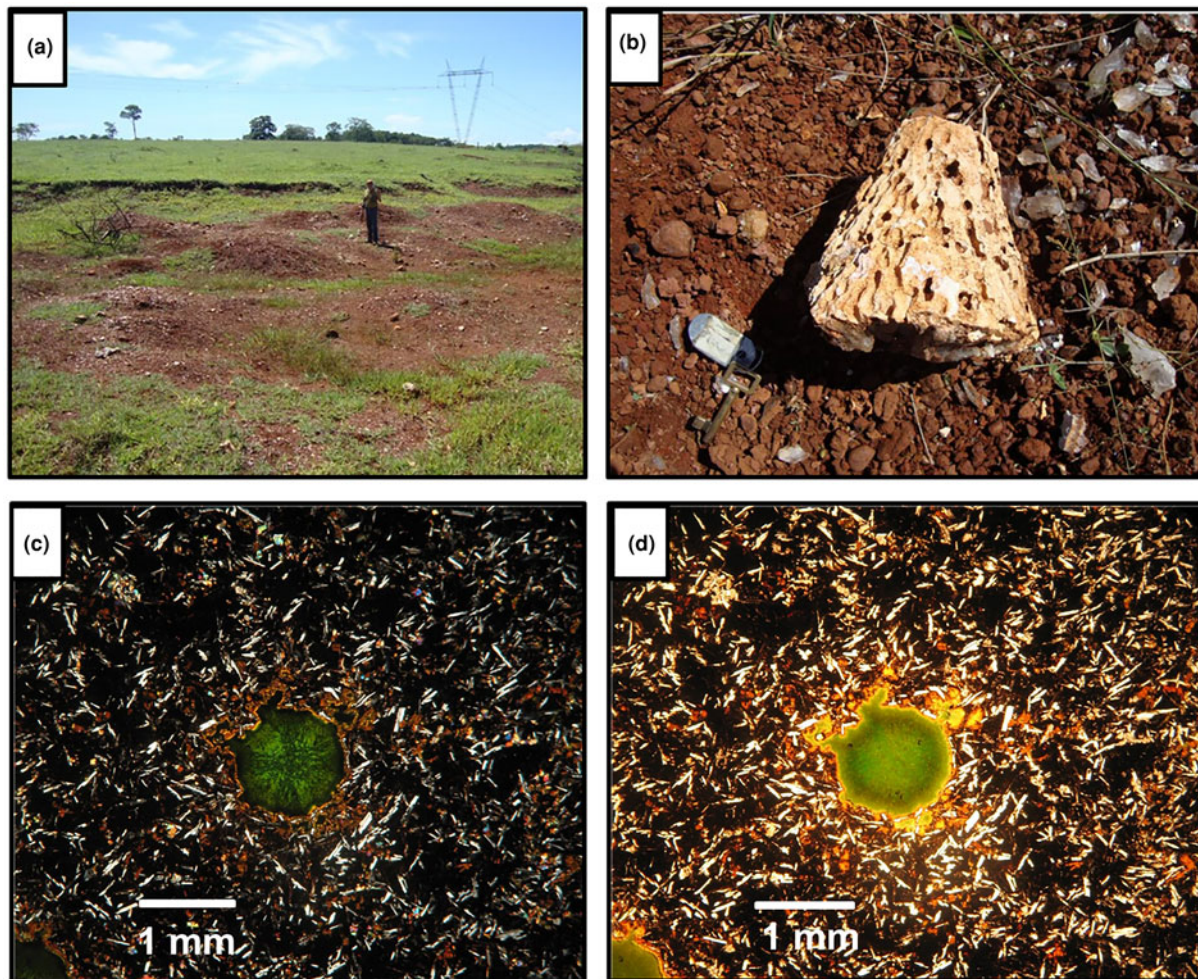


**Fig. 5.** (a) General view of the regolith from which amethyst crystals were recovered; (b) geode fragment typical for this locality, with conical shape; (c) general aspect of the host rock matrix, composed of plagioclase, clinopyroxene and glass, with smectite filling a cavity (crossed polarisers); and (d) same specimen in plane polarised light .

the exact origin of these types of crystals, so this sample was selected from a known occurrence outside Minas Gerais. This region consists of granitic and gneissic rocks and is located in the Eastern Brazilian Pegmatite Province, which covers an area of  $\sim 150,000$  km<sup>2</sup>. The pegmatite bodies are related to the granitic magmatism developed during the Araçuaí Orogeny (Pedrosa-Soares *et al.*, 2011). Granitic rocks, including pegmatites, have ages ranging from the end of the Neoproterozoic to the Cambro–Ordovician and cover around one third of this region (Dardenne and Schobbenhaus, 2003; Pedrosa-Soares *et al.*, 2009). Vieira *et al.* (2013) identified syn- to post-orogenic granitic intrusive rocks from Neoproterozoic and Cambrian suites around Pancas.

The Pancas amethyst occurrence is located at the Itajobi Farm, where post-collisional Carlos Chagas Batolith crops out. In this region, pegmatites are usually tabular, up to 2 m in thickness and poorly differentiated, with no apparent zoning. Aquamarine and chrysoberyl are the main products of the local mining activity, extracted from both altered pegmatites and secondary alluvial deposits. Amethyst, in addition to milky, hyaline, smoky and morion quartz varieties, occurs in cavities covered with druses in intensely weathered pegmatites, or associated with placer deposits. The samples collected from the cavities show massive hyaline quartz at the base, on which the amethyst crystals and

several parallel lines of solid hematite inclusions have overgrown (Fig. 3).

## Results

### *Mapping and classification of fluid inclusions*

#### *Basalt cavity amethyst – T1*

Sample T1 presents only one-phase aqueous inclusions (Fig. 9), which do not allow homogenisation temperatures to be obtained from heating tests and consequently, will not be considered further. The fluid inclusions are rounded and generally elongated, with a larger dimension between 100 and  $<1$   $\mu\text{m}$ , arranged in trails and clouds inside the crystal (Fig. 9a) or filling healed fractures with necking-down features such as elongated shape, sharp edges and signs that the fluids inside the inclusion have leaked (Fig. 9b). They were classified as pseudo-secondary. Moreover, the absence of primary fluid inclusions could be explained by a post-crystallisation deformational event.

#### *Hydrothermal vein amethyst – FS1 and FS2*

Sample FS1 (Fig. 10) has both one-phase and two- or three-phase fluid inclusions. The thin section investigated was made from a

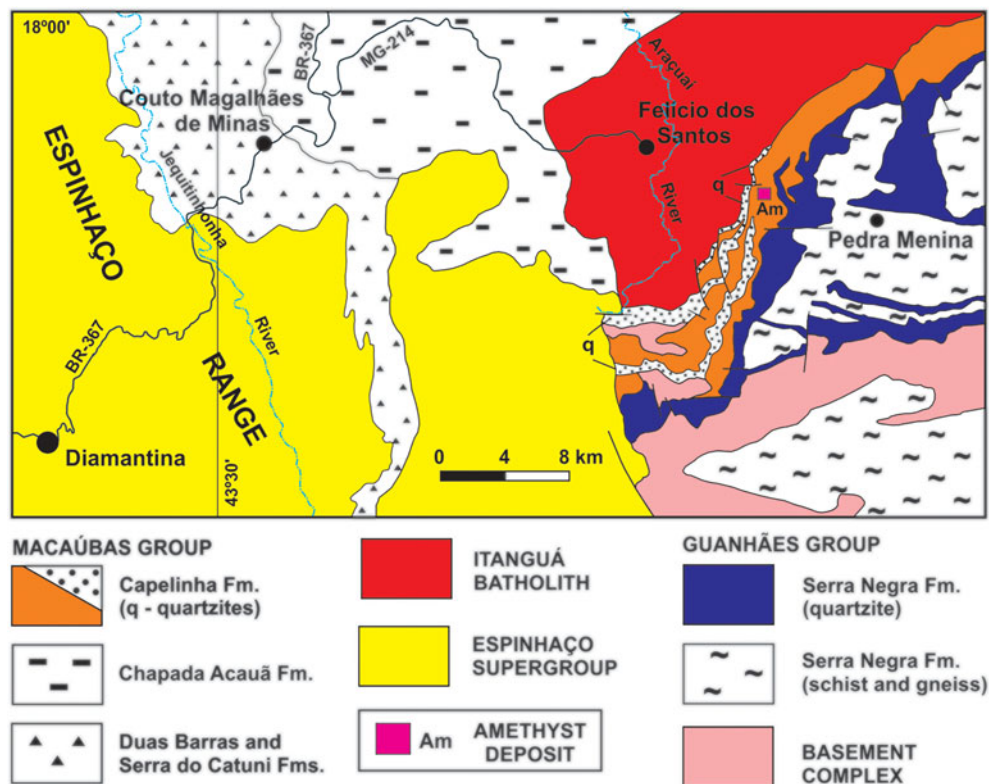


Fig. 6. Simplified geological context of Felício dos Santos region. Based on Tupinambá *et al.* (2012) and Fogaça (2012).

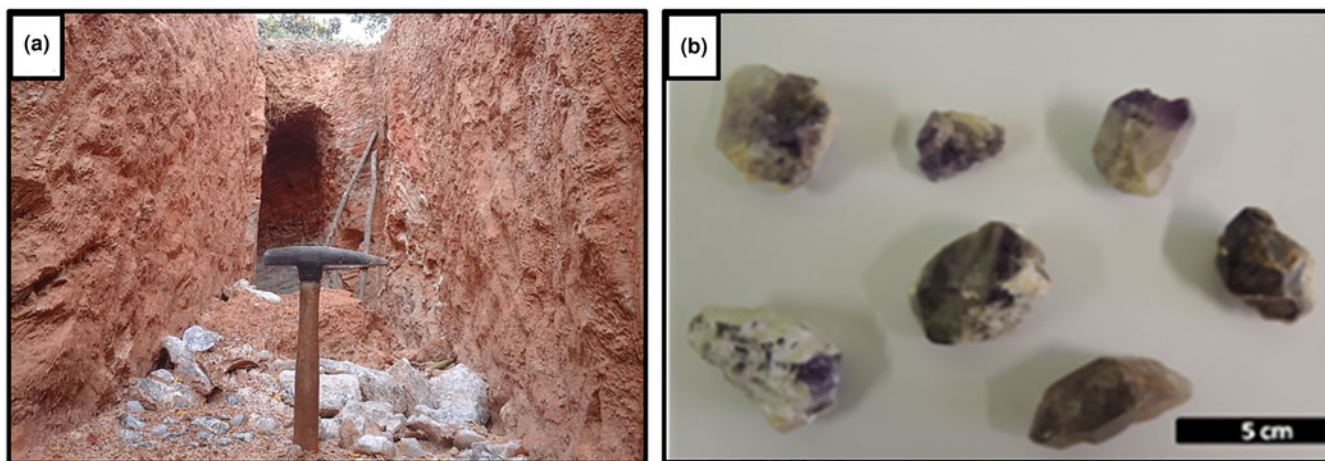


Fig. 7. (a) Recent excavations at Sobrado Farm, Felício dos Santos, in extensively weathered mica-quartz schist, with milky and hyaline quartz fragments; (b) amethyst samples associated with kaolin and milky or colourless quartz. The upper termination of the crystals has a dark violet colour.

single crystal. The approximate  $c$  axis direction is shown on Fig 10a. Several trails parallel to this direction were observed through the smallest magnification of the petrographic microscope ( $\times 2.5$ ). Several other trails are observed perpendicular or oblique to the first ones, in addition to fractures without preferential direction. These are indicative of possible deformation processes after the mineral crystallisation. Most of the inclusions on these trails are not preserved, which could be explained by stretching and decrepitation of fluid inclusions during post-trapping deformation.

The main fluid inclusions within sample FS1 (Figs 10, 11) are classified as types I, II, III and IV. In this sample, type I inclusions

are three-phase aqueous carbonic (water, liquid  $\text{CO}_2$  and vapour), with a variable  $\text{CO}_2$  volume ratio of 50–80% in relation to total inclusion volume. They are polygonal-to-elongated with the largest dimension reaching  $50\ \mu\text{m}$ , commonly with negative crystal shapes. Type I inclusions are distributed in planes, clusters or trails that are limited to the interior of the crystal, being classified as pseudo-secondary (Fig. 11).

Most inclusions are two-phase aqueous fluid inclusions, with low vapour ratios of 5–20% in relation to total inclusion volume. Based on heating test results, these inclusions were differentiated as types II (high  $T$ , with homogenisation temperatures above  $249^\circ\text{C}$ ) and III

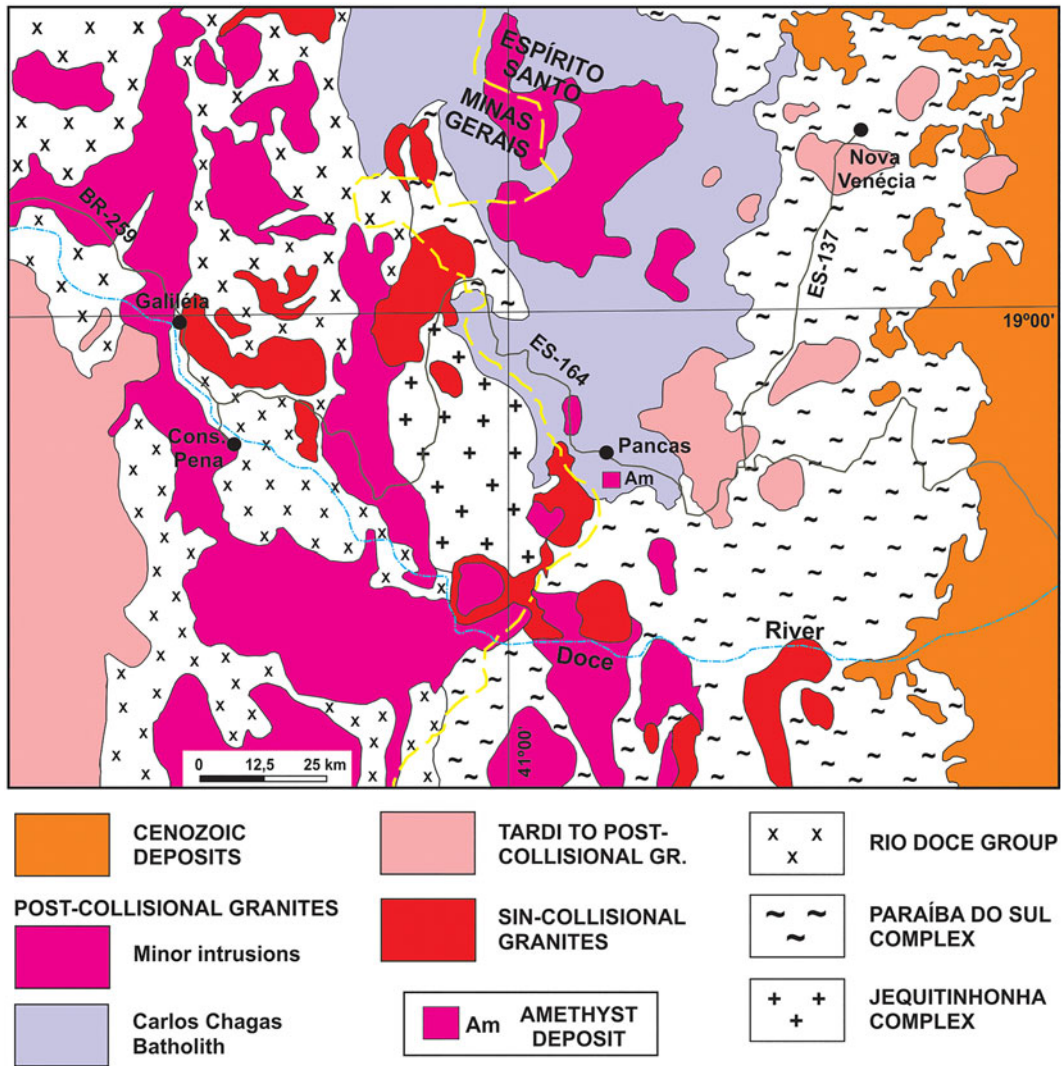


Fig. 8. Simplified geological context of the Pancas region. Based on Leite *et al.* (2004).

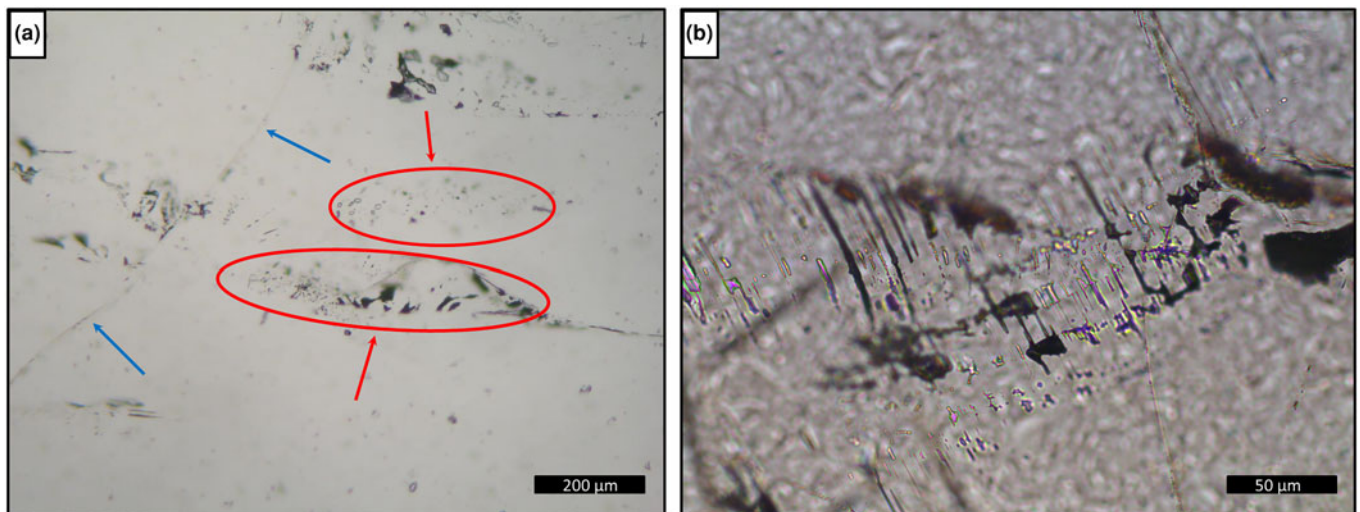
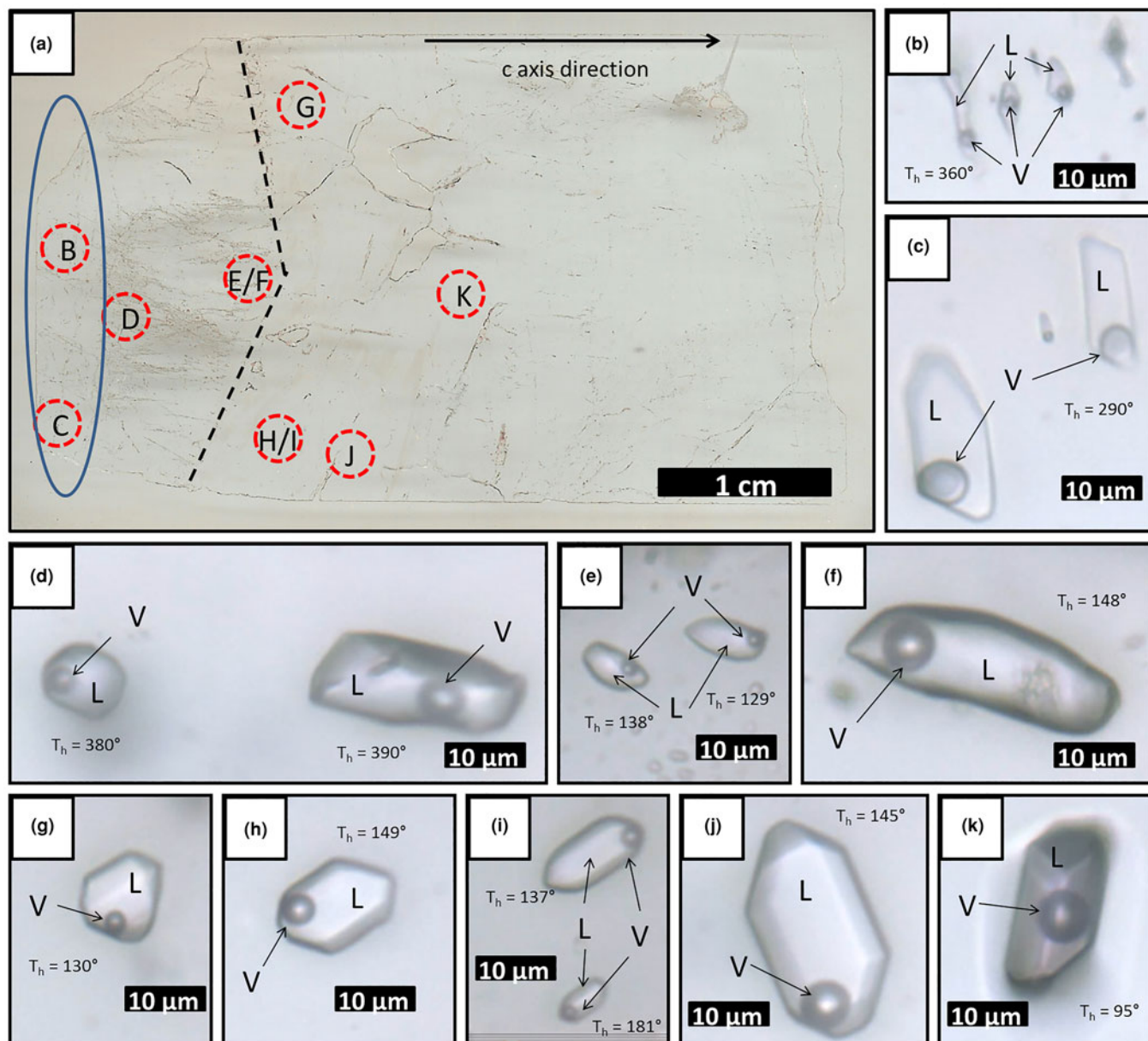


Fig. 9. Photomicrographies of fluid inclusions in basalt cavity amethyst, sample T1: (a) trails (blue arrows) and clouds (red arrows and ellipses) of one-phase inclusions inside the crystal; and (b) detail of elongated one-phase inclusions with necking-down features.



**Fig. 10.** (a) Scanned surface of hydrothermal vein sample FS1, showing location of photomicrographs B to K; (b–d) type II two-phase aqueous fluid inclusions ( $\times 100$  zoom); (e–k) type III two-phase aqueous fluid inclusions ( $\times 100$  zoom). Dashed line shows a growth zone; ellipse delimitates the region of occurrence of aqueous carbonic inclusions. L: aqueous liquid; V: water vapour;  $T_h$ : total homogenisation temperature.

(low  $T$ , with homogenisation temperatures below  $203^\circ\text{C}$ ). Type II inclusions are rounded to polygonal, elongated or irregular, and can be up to  $70\ \mu\text{m}$  in length. They are distributed in planes or trails that are limited to the interior of the crystal and are classified as pseudo-secondary. They only occur at the base of the crystal, before the growth line shown on Fig. 10a. Type III inclusions are rounded to polygonal, elongated or negative crystal shape, and can be up to  $150\ \mu\text{m}$  in length. They are distributed in planes or trails that are limited to the interior of the crystal and are also classified as pseudo-secondary. Unlike type II inclusions, they occur after, or close to, the growth line shown on Fig. 10a. Type IV inclusions are one-phase aqueous, rounded to elongated or irregular in shape, and up to  $30\ \mu\text{m}$  in length. They are preferentially distributed in trails cutting through the crystal or planes of different depths within it, and are classified as secondary.

Fluid inclusions can locally show necking-down features, such as elongated shape, sharp edges and signs that the fluid inside the inclusion has leaked, which may suggest deformation after their trapping. These inclusion types were not considered. No inclusions were classified as primary because characteristics such as preserved inclusions in growth zones, or isolated inclusions were not easy to distinguish. The microthermometric measurements were performed only in types I, II and III inclusions, classified as pseudo-secondary that would be related to the crystallisation conditions of the amethyst. Sample FS2 contains both one-, two- and three-phase fluid inclusions, with dominant one-phase aqueous inclusions. The thin section studied was made from a single crystal (Fig. 12). The main types of fluid inclusions are described as types I, II and III. Type I inclusions are three-phase aqueous carbonic (water, liquid  $\text{CO}_2$  and vapour), with a



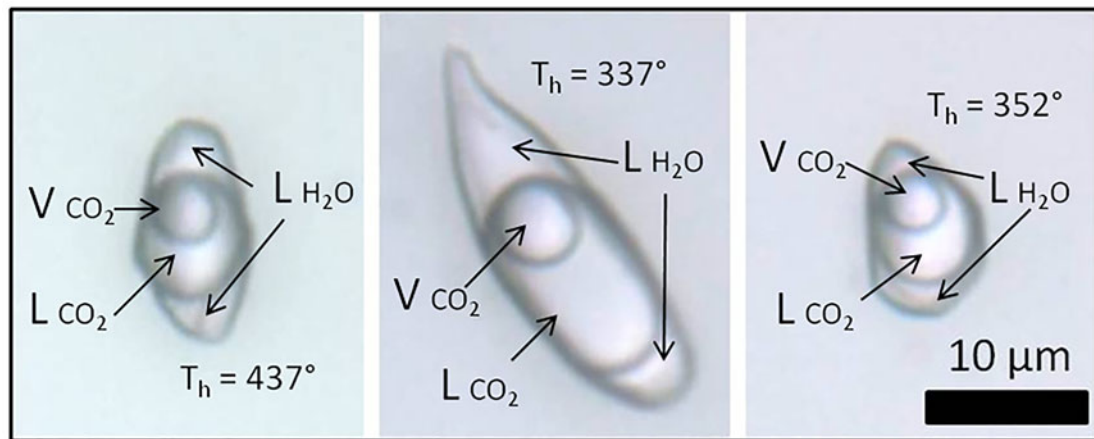


**Fig. 11.** Photomicrographies of type I three-phase aqueous-carbonic fluid inclusions trapped in amethyst quartz from hydrothermal vein sample FS1.  $L_{H_2O}$ : aqueous liquid;  $L_{CO_2}$ :  $CO_2$  liquid;  $V_{CO_2}$ :  $CO_2$  vapour;  $T_h$ : total homogenisation temperature.

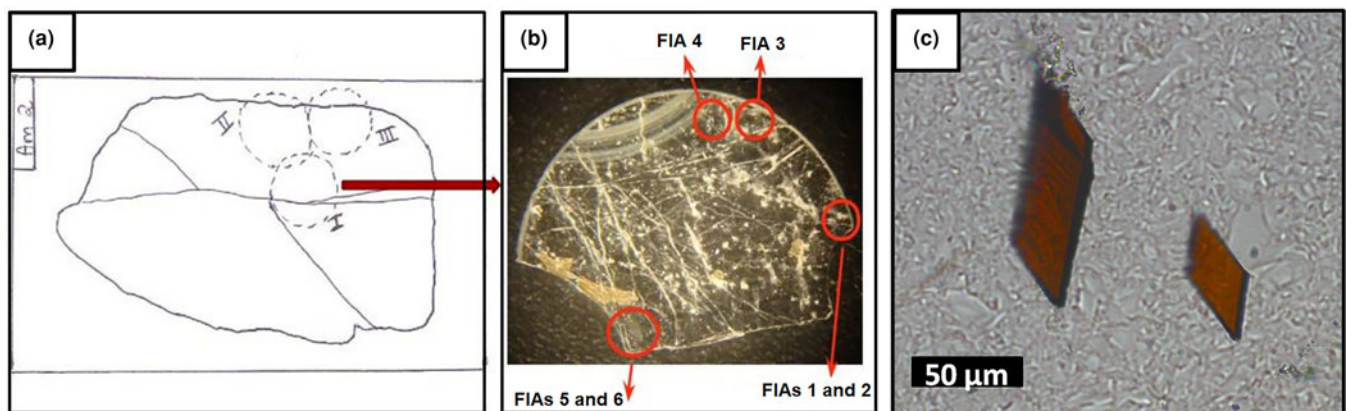


**Fig. 12.** (a) Thin section sketch of hydrothermal vein sample FS2, with significant fractures and regions selected for cutting; (b) chip I after making the cuts with a cutting wheel, in the regions indicated in (a), showing FIAs measured; and (c) photomicrograph of hematite solid inclusions observed in this sample.

high  $CO_2$  volume ratio of 70–90% of total inclusion volume. These are polygonal-to-elongated, commonly with a negative crystal shape, and can reach 100  $\mu m$  in the largest dimension. Type I inclusions are distributed along planes, clusters or trails that are limited to the interior of the crystal, and are classified as pseudo-secondary (Fig. 13a–d).

Type II are two-phase aqueous fluid inclusions, with low vapour ratios of 5–10% of the total inclusion volume. Those inclusions are polygonal, elongated or irregular, and can be up to 70  $\mu m$  in length. They are distributed in planes or trails that are limited to the interior of the crystal, being classified as pseudo-secondary (Fig. 8e). Type III inclusions are one-phase aqueous, rounded-to-elongated or irregular in shape, and up to 30  $\mu m$  in length. They are distributed mostly in trails that cut through the crystal, or planes of different depths within it, and are classified as secondary (Fig. 13f).

The fluid inclusions of the three types described can also show necking-down features. Types II and III inclusions are generally small and phase changes are difficult to observe. Thus, the microthermometric measurements were performed only in the type I inclusions, classified as pseudo-secondary. Numerous hematite solid inclusions can be observed with the naked eye inside the crystals (Fig. 12c).

#### *Pegmatite amethyst – P1*

Fluid inclusions trapped in sample P1 (Fig. 14) occur as trails or clusters with different spatial orientations. The thin section studied was cut from a crystal aggregate with hyaline quartz at its base and amethyst at the top. An approximate  $c$  axis direction is shown on Fig 14a. The two types of quartz are separated by a rough band of hematite solid inclusions. Several other hematite inclusions are observed perpendicular to growth zones and most of the inclusions on these zones are not preserved.

The fluid inclusions are described as types I, II, III and IV. Type I inclusions are three-phase aqueous carbonic (water, liquid  $CO_2$  and vapour), with a  $CO_2$  volume ratio of 90–95% of the total inclusion volume. They are polygonal-to-elongated, commonly with negative crystal shapes, and can reach up to 150  $\mu m$ . These are distributed in clouds or trails that are limited to the interior of the crystal, being classified as pseudo-secondary (Fig. 14d).

Type II are three-phase (liquid, vapour and solid) aqueous fluid inclusions with precipitated halite, showing a low vapour ratio of 5–10% in relation to the total inclusion volume. They have rounded-to-polygonal, elongated or irregular shapes, with sizes reaching up to 280  $\mu m$ , although larger inclusions are almost always stretched. Type II inclusions are distributed in clusters or trails that are limited to the interior of the crystal, and are

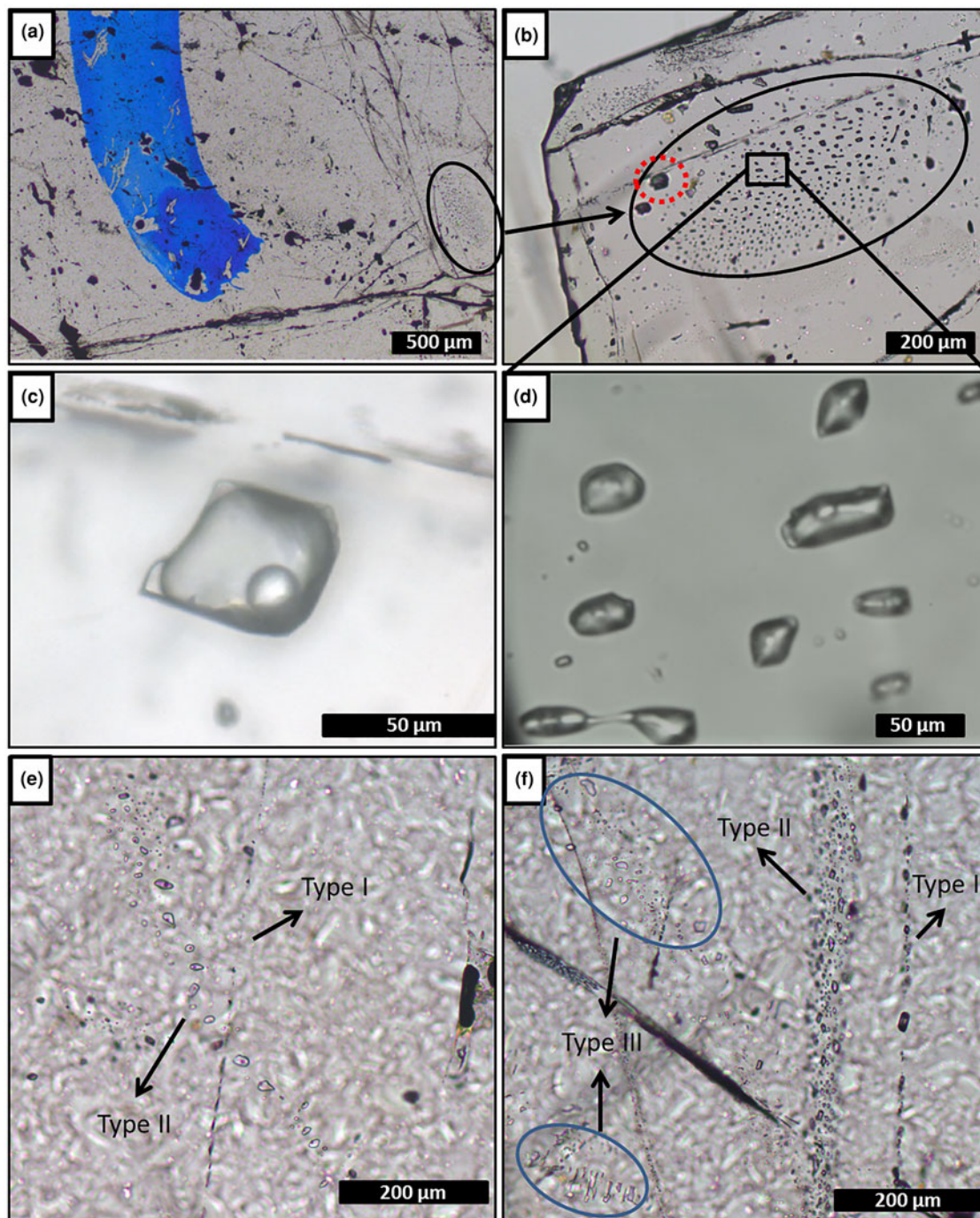


**Fig. 13.** (a) Hydrothermal vein sample FS2, showing part of chip I and blue mark where the chip was cut, FIA 5 delineated on the right ( $\times 2.5$  zoom); (b) type I three-phase aqueous-carbonic inclusions cloud – FIA 5, red dashed line marks the inclusion shown in (c) ( $\times 10$  zoom); (c) FIA 5 inclusion in detail ( $\times 50$  zoom); (d) FIA 5 inclusions in detail ( $\times 100$  zoom); (e) FIA of type II two-phase aqueous inclusions crosscutting a FIA of type I very small aqueous-carbonic inclusions ( $\times 10$  zoom); and (f) clusters of type III one-phase aqueous inclusions and trails of types II and III inclusions.

classified as pseudo-secondary (Fig. 14b). Two-phase aqueous (liquid and vapour) inclusions also occur. On the basis of heating test results, they were separated into types III (high  $T$ , with homogenisation temperatures above  $268^{\circ}\text{C}$ ) and IV (low  $T$ , with homogenisation temperatures below  $247^{\circ}\text{C}$ ). Both type III and type IV fluid inclusions have rounded-to-polygonal, elongated or irregular shapes. These are also distributed in clusters or trails that are limited to the interior of the crystal, being classified as pseudo-secondary (Fig. 14c).

#### *Microthermometry of the fluid inclusions*

Data obtained from freezing and heating experiments are summarised on Tables 2, 3 and 4. It was difficult to determine the eutectic melting temperature ( $T_e$ ) in most of the observed inclusions, however, an estimation of the  $T_e$  of  $\text{H}_2\text{O}-\text{NaCl}$  ( $-21.2^{\circ}\text{C}$ ) was used to discriminate the presence of other cations in addition to Na in aqueous inclusions from both hydrothermal vein and pegmatite samples (Fig. 15a). Eutectic temperatures below  $-30^{\circ}\text{C}$  were observed in samples FS1 (types II and III) and P1 (types II, III and IV), and below

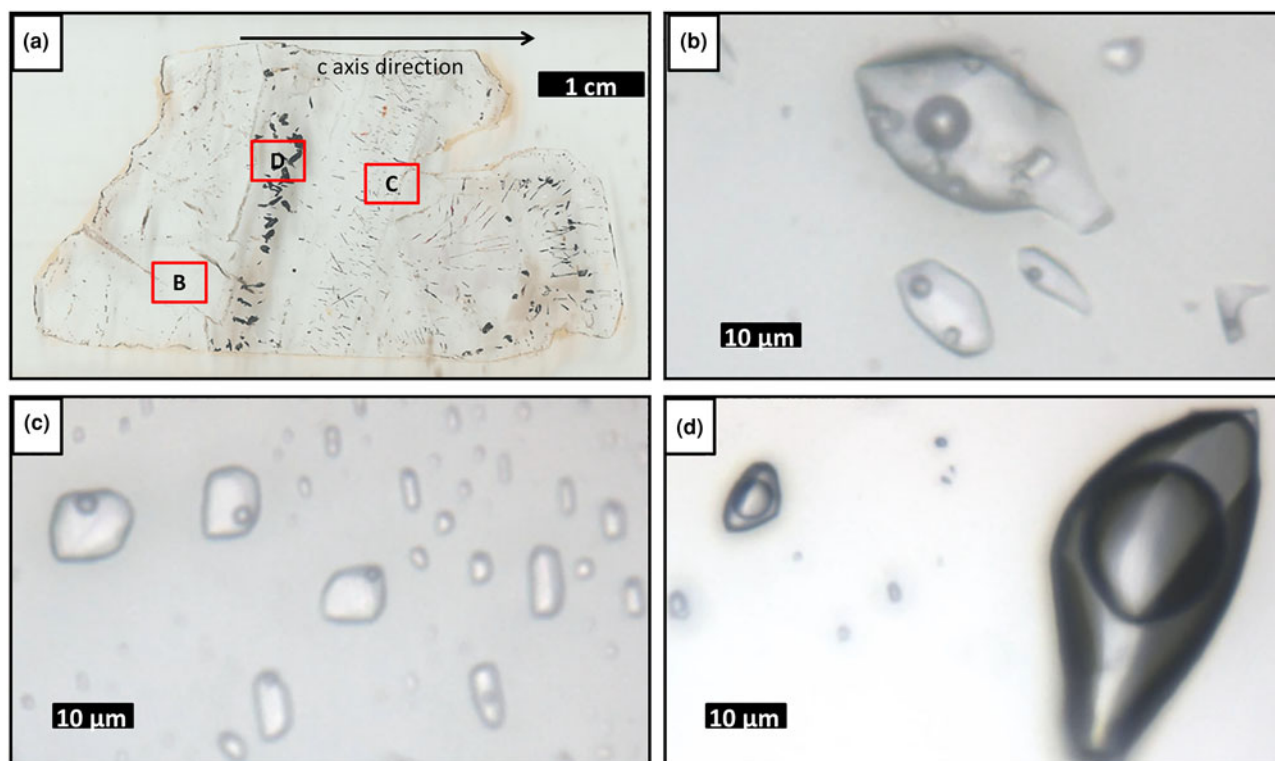


**Fig. 14.** (a) Pegmatite sample P1, showing location of (b), (c) and (d); (b) type II three-phase aqueous inclusions FIA; (c) type III two-phase aqueous inclusions FIA; and (d) type I three-phase aqueous-carbonic inclusions FIA.

**Table 2.** Microthermometric results of pseudo-secondary fluid-inclusion assemblages in amethyst samples from Felício dos Santos' hydrothermal vein (FS1).

Fluid-inclusion types	Shape	Occurrence	Microthermometric data
<b>Type 1</b> Three-phase ( $L_{H_2O} + L_{CO_2} + V_{CO_2}$ ) aqueous carbonic FIs 1–50 $\mu\text{m}$ 50 to 80 $\text{CO}_2$ vol.%	Polygonal, elongated or negative crystal shape	Planes, clusters or trails limited to the interior of the crystals	$T_{mCO_2}$ : –56.3 to –57.6°C ( $N = 36;13$ ) $T_{clath}$ : 8.8 to 7.4°C ( $N = 36;13$ ) $T_{hCO_2-L}$ : 26.5 to 30.9°C ( $N = 36;13$ ) Salinity: 2.4 to 5.0 eq. wt.% NaCl (mean 3.6; $N = 36;13$ ) Density: 0.53 to 0.82 $\text{g}/\text{cm}^3$ ( $N = 36;13$ ) $T_{htot-L}$ : 373°C ( $N = 1$ )
<b>Type 2</b> Two-phase ( $L_{H_2O} + V_{H_2O}$ ) liquid-rich aqueous FIs with $T_{htot} > 249^\circ\text{C}$ 1–70 $\mu\text{m}$ ; $F = 0.8\text{--}0.95$	Rounded to polygonal, elongated or irregular shape	Planes or trails limited to the interior of the crystals	$T_{mice}$ : –6.4 to –2.1°C (mean –4°C; $N = 42;19$ ) Salinity: 3.4 to 9.7 eq. wt.% NaCl (mean 6.3; $N = 36;13$ ) Density: 0.58 to 0.88 $\text{g}/\text{cm}^3$ ( $N = 16;12$ ) $T_{htot-L}$ : 249 to 391°C (mean 329.3°C; $N = 16;12$ ) $T_e$ : –37 to –10°C (mean –29.2°C; $N = 19;9$ )
<b>Type 3</b> Two-phase ( $L_{H_2O} + V_{H_2O}$ ) liquid-rich aqueous FIs with $T_{htot} < 203^\circ\text{C}$ 1–150 $\mu\text{m}$ ; $F = 0.8\text{--}0.95$	Elongated, rounded or negative crystal shape	Planes or trails limited to the interior of the crystals	$T_{mice}$ : –2.8 to –7.8°C (mean –5.4°C; $N = 68;23$ ) Salinity: 4.6 to 11.5 eq. wt.% NaCl (mean 8.3; $N = 68;23$ ) Density: 0.93 to 1.01 $\text{g}/\text{cm}^3$ ( $N = 43;17$ ) $T_{htot-L}$ : 82 to 203°C (mean 137.2°C; $N = 46;18$ ) $T_e$ : –55 to –35°C (mean –41°C; $N = 36;15$ )

L: liquid; V: vapour; F: degree of fill; N: number of inclusions measured; number of FIAs;  $T_{mCO_2}$ :  $\text{CO}_2$  melting temperature;  $T_{clath}$ : temperature of clathrate melting;  $T_{hCO_2-L}$ : homogenisation temperature of  $\text{CO}_2$  phases to liquid;  $T_e$ : temperature of first ice melting;  $T_{mice}$ : temperature of last ice melting;  $T_{htot-L}$ : homogenisation temperature to liquid phase.

–50°C in samples FS1 (type III) and P1 (types II, III and IV), indicating the presence of cations such as Ca and Fe other than Na. Also, eutectic temperatures around –11°C observed in type II fluid inclusions from sample FS1 could indicate the presence of a  $\text{H}_2\text{O}$ –KCl system composition.

A homogenisation temperature was only observed in some aqueous carbonic inclusions, as the separation between aqueous and carbonic phases seem to remain until the end of heating tests and most inclusions decrepitated during other tests.

Consequently, few homogenisation temperatures could be determined for these types of inclusions. Due to the decrepitation of many fluid inclusions during the heating tests, only 99 homogenisation temperature measurements were obtained, most of them in aqueous inclusions (Fig. 15d).

#### Hydrothermal vein amethyst – FS1 and FS2

In sample FS1, type I inclusions show salinity values varying from 2.4 to 5.0 eq. wt.% NaCl. Only one homogenisation temperature

**Table 3.** Microthermometric results of pseudo-secondary fluid-inclusion assemblages in amethyst samples from Felício dos Santos' hydrothermal vein (FS2).

Fluid-inclusion types	Shape	Occurrence	Microthermometric data
Type 1 Three-phase (L <sub>H<sub>2</sub>O</sub> + L <sub>CO<sub>2</sub></sub> + V <sub>CO<sub>2</sub></sub> ) aqueous carbonic FIs 1–100 μm 70 to 90 CO <sub>2</sub> vol.%	Polygonal, elongated or negative crystal shape	Planes, clusters or trails limited to the interior of the crystals	T <sub>mCO<sub>2</sub></sub> : –56.7 to –61.4°C (N = 29;10) T <sub>clath</sub> : 8.6 to 4.9°C (N = 29;10) T <sub>hCO<sub>2</sub></sub> – L: 17.3 to 28.5°C (N = 29;10) Salinity: 2.8 to 9.1 eq. wt.% NaCl (mean 5.0; N = 29;10) Density: 0.7 to 0.9 g/cm <sup>3</sup> (N = 29;10) T <sub>htot</sub> – L: 210 to 270°C (mean 228.3°C; N = 6;3)

L: liquid; V: vapour; N: number of inclusions measured; number of FIAs; T<sub>mCO<sub>2</sub></sub>: CO<sub>2</sub> melting temperature; T<sub>clath</sub>: temperature of clathrate melting; T<sub>hCO<sub>2</sub></sub> – L: homogenisation temperature of CO<sub>2</sub> phases to liquid; T<sub>htot</sub> – L: homogenisation temperature to liquid phase.

**Table 4.** Microthermometric results of pseudo-secondary fluid-inclusion assemblages in amethyst samples from Pancas pegmatite (P1).

Fluid-inclusion types	Shape	Occurrence	Microthermometric data
Type 1 Three-phase (L <sub>H<sub>2</sub>O</sub> + L <sub>CO<sub>2</sub></sub> + V <sub>CO<sub>2</sub></sub> ) aqueous carbonic FIs 1–150 μm 90 to 95 CO <sub>2</sub> vol.%	Polygonal, elongated or negative crystal shape	Clusters or trails limited to the interior of the crystals	T <sub>mCO<sub>2</sub></sub> : –56.7 to –58.4°C (N = 4;3) T <sub>clath</sub> : 8.7 to 5.2°C (N = 4;3) T <sub>hCO<sub>2</sub></sub> – L: 21.6 to 24.3°C (N = 4;3) Salinity: 2.6 to 8.7 eq. wt.% NaCl (mean 4.8; N = 4;3) Density: 0.75 to 0.77 g/cm <sup>3</sup> (N = 4;3) T <sub>htot</sub> – L: 160°C (N = 1)
Type 2 Three-phase (L <sub>H<sub>2</sub>O</sub> + V <sub>H<sub>2</sub>O</sub> + S) liquid-rich aqueous FIs with halite 1–280 μm; F = 0.9–0.95	Rounded to polygonal, elongated or irregular shape	Clusters or trails limited to the interior of the crystals	T <sub>mice</sub> : –13.9 to –19.8°C (mean –16.9°C; N = 8;3) T <sub>mHH</sub> : –12.5 to –19.0°C (mean –16.0°C; N = 10;4) Salinity: 38.7 eq. wt.% NaCl (N = 1) Density: 1 to 1.10 g/cm <sup>3</sup> (N = 3;2) T <sub>htot</sub> – L: 133 to 147°C (mean 142°C; N = 3;2) T <sub>e</sub> : –56 to –54°C (mean –54.4°C; N = 15;5)
Type 3 Two-phase (L <sub>H<sub>2</sub>O</sub> + V <sub>H<sub>2</sub>O</sub> ) liquid-rich aqueous FIs with T <sub>htot</sub> > 268°C 1–80 μm; F = 0.8–0.95	Rounded to polygonal, elongated or irregular shape	Clusters or trails limited to the interior of the crystals	T <sub>mice</sub> : –7 to –19.1°C (mean –13.1°C; N = 14;5) T <sub>mHH</sub> : –1.1°C (N = 1) Salinity: 10.5 to 26.1 eq. wt.% NaCl (mean 17.3; N = 15;6) Density: 0.71 to 0.96 g/cm <sup>3</sup> (N = 5;3) T <sub>htot</sub> – L: 268 to 375°C (mean 337.8°C; N = 5;3) T <sub>e</sub> : –58 to –49°C (mean –53.5°C; N = 11;6)
Type 4 Two-phase (L <sub>H<sub>2</sub>O</sub> + V <sub>H<sub>2</sub>O</sub> ) liquid-rich aqueous FIs with T <sub>htot</sub> < 247°C 1–150 μm; F = 0.8–0.95	Rounded to polygonal, elongated or irregular shape	Clusters or trails limited to the interior of the crystals	T <sub>mice</sub> : –5 to –17.9°C (mean –14.3°C; N = 26;10) T <sub>mHH</sub> : –8.8 to –20.6°C (mean –15.9°C; N = 15;3) Salinity: 7.8 to 24.8 eq. wt.% NaCl (mean 20.6; N = 41;13) Density: 0.96 to 1.08 g/cm <sup>3</sup> (N = 24;10) T <sub>htot</sub> – L: 125 to 247°C (mean 162.8°C; N = 24;10) T <sub>e</sub> : –55 to –54°C (mean –54.5°C; N = 37;13)

L: liquid; V: vapour; F: degree of fill; N: number of inclusions measured; number of FIAs; T<sub>mCO<sub>2</sub></sub>: CO<sub>2</sub> melting temperature; T<sub>clath</sub>: temperature of clathrate melting; T<sub>hCO<sub>2</sub></sub> – L: homogenisation temperature of CO<sub>2</sub> phases to liquid; T<sub>e</sub>: temperature of first ice melting; T<sub>mice</sub>: temperature of last ice melting; T<sub>mHH</sub>: temperature of hydrohalite melting; T<sub>htot</sub> – L: homogenisation temperature to liquid phase.

of 373°C was observed (Table 2) through expansion of the CO<sub>2</sub> phase (Table 2). Salinities were obtained from clathrate melting temperatures. For type II inclusions, the salinities were obtained from ice melting temperatures and vary in a wider range between 3.4 and 9.7 eq. wt.% NaCl. Homogenisation temperatures, observed through homogenisation into the liquid phase, vary between 249°C and 391°C (Fig. 15d, Table 2). Salinity values for type III inclusions were also obtained from ice melting temperatures, and range between 4.6 and 11.5 eq. wt.% NaCl. Homogenisation to a liquid phase was observed at temperatures ranging from 82°C to 203°C. For type I inclusions within sample FS2, the salinities obtained from clathrate melting temperatures are between 2.8 and 9.1 eq. wt.% NaCl, with homogenisation temperatures varying between 210°C and 270°C (Fig. 15d, Table 3) observed through expansion of the CO<sub>2</sub> phase.

#### Pegmatite amethyst – P1

Type I inclusions have salinities between 2.6 and 8.7 eq. wt.% NaCl, obtained from clathrate melting temperatures. Only one homogenisation temperature of 160°C (Table 4) was observed through expansion of the CO<sub>2</sub> phase. For type II inclusions, only one salinity value of 38.71 eq. wt.% NaCl was obtained, through observation of the halite final dissolution temperature. Other inclusions do not show dissolution of solid phases until greater than 400°C. Partial homogenisation temperatures (homogenisation of liquid and vapour phases) vary between 133°C and 147°C (Fig. 15d, Table 4) and were observed through homogenisation into a liquid phase. Type III inclusions show salinities varying in a wider range from 10.5 to 26.1 eq. wt.% NaCl, obtained from ice or hydrohalite melting temperatures, and homogenisation temperatures between 268°C and 375°C

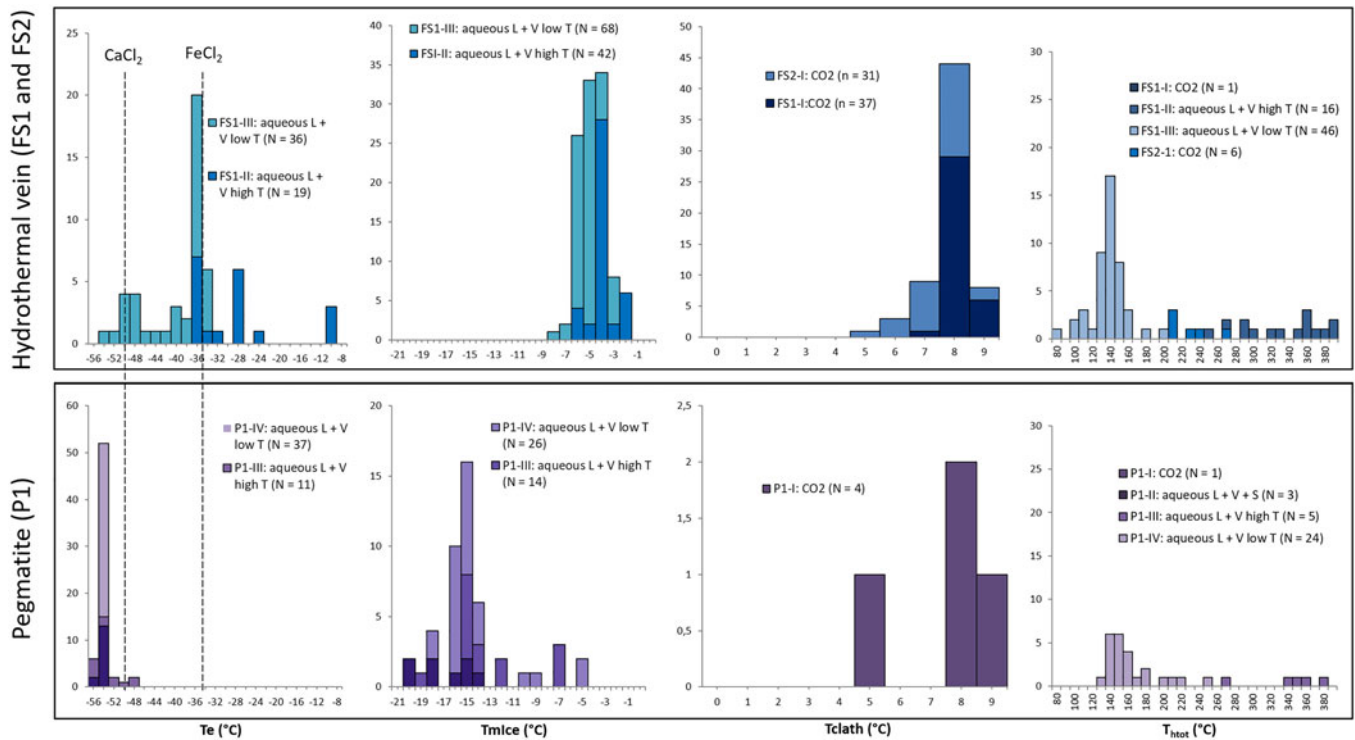


**Fig. 15.** Histograms of: eutectic ( $T_e$ ); final ice melting ( $T_{mice}$ ); clathrate melting ( $T_{clath}$ ); and total homogenisation temperatures ( $T_{htot}$ ) for the samples from hydrothermal vein (FS1 and FS2) and pegmatite (P1).

(Fig. 15, Table 4) observed through homogenisation into a liquid phase.

### Raman spectroscopy of the fluid inclusions

#### Hydrothermal vein amethyst – FS2

As the measured  $\text{CO}_2$  melting temperatures are below the expected value of  $-56.6^\circ\text{C}$  (between  $-56.3^\circ\text{C}$  and  $-61.4^\circ\text{C}$ , with average value of  $-57.3^\circ\text{C}$ ), the presence of different gases dissolved within the carbonic phase is suggested, e.g.  $\text{CH}_4$ , as it could result in lower  $\text{CO}_2$  melting temperatures. In order to run Raman spectroscopic analyses, the sample FS2 was chosen because of its high content of aqueous carbonic inclusions. Carbonic inclusions of larger size were selected to aid laser positioning. The spectra shown in Fig. 16 confirms the presence of gaseous  $\text{CO}_2$  with the peaks at  $1285$  and  $1388\text{ cm}^{-1}$  (stretching vibrations), but do not show the main  $\text{CH}_4$  peak at  $2917\text{ cm}^{-1}$  (Frezzotti *et al.* 2012). Therefore, it was considered that carbonic phases are composed of pure  $\text{CO}_2$  for further calculations. Bands other than  $1285$  and  $1388\text{ cm}^{-1}$  were also present in quartz Raman spectra, and were assigned to the fluid-inclusions host mineral.

### Discussion

Mapping of the basalt cavity amethyst sample (T1) revealed mostly one-phase aqueous fluid inclusions suggesting a low-temperature formation environment for this type of amethyst. This is corroborated by the data of Juchem (1999), who described samples of amethyst from volcanic rocks of Rio Grande do Sul State. Fluid-inclusion data from Gilg *et al.* (2003, 2012), also from amethyst in basaltic geodes from Rio Grande do Sul, indicate temperatures below  $100^\circ\text{C}$  during filling of the geodes, similarly to the results presented by Commin-Fischer *et al.* (2010). These authors

have described the crystallisation of amethyst in this type of environment with low-salinity fluids, between 2 and 8 eq. wt.% NaCl.

Samples from the hydrothermal veins (FS1 and FS2) show salinities varying between 2.4 and 12.5 wt.%, representing low-to-moderate salinity fluids. At least two generations of fluids can be considered. The first, containing both aqueous and carbonic phases, have minimum trapping temperatures between  $249^\circ\text{C}$  and  $391^\circ\text{C}$ . Lower eutectic temperatures observed in aqueous inclusions with higher homogenisation temperatures indicate other cations such as Fe in addition to Na. The carbonic composition of the system  $\text{H}_2\text{O}-\text{CO}_2-\text{NaCl}$ , which was confirmed by Raman spectroscopy analyses, suggests a metamorphic and/or magmatic source for the fluids. Metamorphic fluids would be originated by regional metamorphism associated with the Araçuaí Orogeny, whereas magmatic fluids would be derived from granitic magmatism generated during the same orogenic process. However, further studies such as oxygen stable isotope analysis are necessary to assess the fluid origin. The second generation of lower-temperature fluids shows minimum trapping temperatures varying from  $82^\circ\text{C}$  to  $203^\circ\text{C}$ . Fluid inclusions of this group record lower eutectic temperatures that indicate the presence of Ca and Fe cations in addition to Na. Amethyst from pegmatite (P1) contains fluid inclusions with variable, though mostly high, salinities of 2.6–38.7 eq. wt.% NaCl. Most salinity values lie between 15 and 25 eq. wt.% NaCl, reflecting an elevated salt content in pegmatitic fluids. These represent residual fluids from the solidification of a magmatic intrusion, generally rich in volatiles, incompatible elements and anions such as  $\text{Cl}^-$  and  $\text{F}^-$  (London and Kontak, 2012). We have interpreted the presence of two generations of fluids for this environment. The first is represented by aqueous fluid inclusions with minimum trapping temperatures ranging from  $268^\circ\text{C}$  to  $375^\circ\text{C}$ . Estimated eutectic temperatures mainly below  $-50^\circ\text{C}$  indicate the presence of Ca cations in addition to

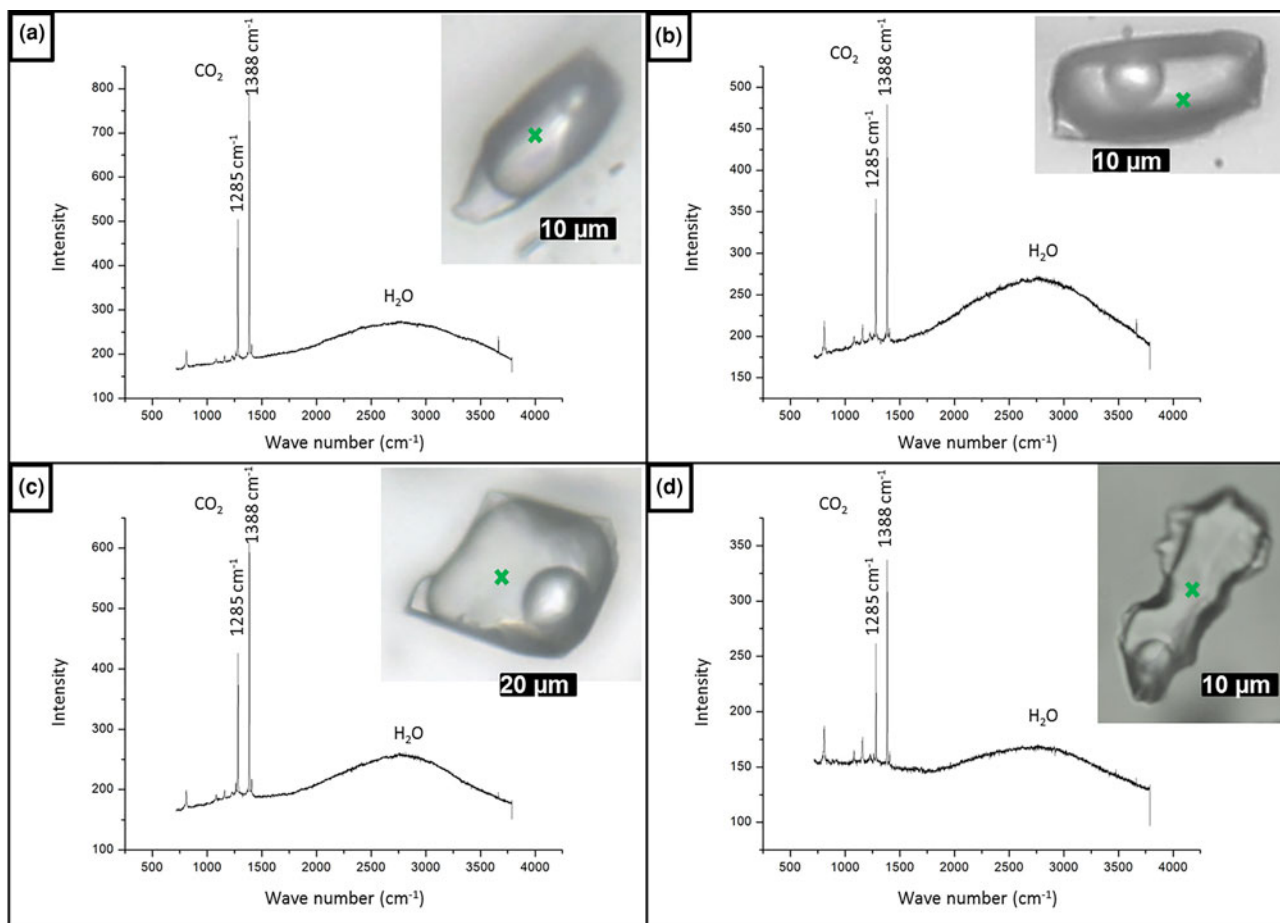


**Fig. 16.** Raman analyses of type I aqueous carbonic inclusions from sample FS2 chip I: (a) FIA 1; (b) FIA 5; (c) FIA 6; and (d) FIA 6a. Green crosses mark approximate analysis spots.

Na. Minimum trapping temperatures correspond possibly to temperatures of late- to post-pegmatitic hydrothermal stages established by Fersmann (1931, in London, 2008). The second fluid generation contains both aqueous and carbonic phases, and records minimum trapping temperatures between 125°C and 247°C. Salinity values of ~38 wt.% eq. NaCl (or even higher) are recorded in three-phase aqueous fluid inclusions with minimum trapping temperatures between 133°C and 147°C. These inclusions have eutectic temperatures around -55°C, also indicating the presence of Ca in the system. The carbonic composition of the system H<sub>2</sub>O-CO<sub>2</sub>-NaCl also indicates a magmatic source for the fluids.

Values of salinity and homogenisation temperatures for both pegmatite and hydrothermal vein samples are plotted on a binary diagram shown on Fig. 17. Sample FS1 displays decreasing homogenisation temperatures, which are delimited by ellipse 1 (high-*T* aqueous inclusions) and ellipse 3 (low-*T* aqueous inclusions) in Fig. 17, whereas sample FS2 shows a narrower range of homogenisation temperatures, delimited by ellipse 2 (medium *T* aqueous carbonic inclusions). In general, samples from hydrothermal veins have a large variation of homogenisation temperatures (82–391°C) with salinity values varying in a narrower range (2.4–11.5 eq. wt.% NaCl); which might represent cooling of the system. Pegmatite sample P1 shows more scattered values with decreasing salinities and homogenisation temperatures, which are mostly located inside the large arrow in Fig. 17.

Such a trend could suggest both cooling of the fluid and mixing with fluids of lower temperature and salinity.

Fluid-inclusion studies in hydrothermal quartz associated with gemmological vein-type titanite mineralisation in the Capelinha region (Chaves *et al.*, 2017), ~90 km from Felício dos Santos, also contain low-salinity fluids (between 0.4 and 2.8 wt.% NaCl), and have minimum trapping temperatures between 300°C and 450°C. Both these hydrothermal vein mineralisations are hosted by metavolcanic schists of the Capelinha Formation, which were further affected by the Araçuaí Orogeny (630–480 Ma). We might relate the hydrothermal fluids responsible for both mineralisations to the same source. According to Chaves *et al.* (2017), the hydrothermal mineralising event of titanite has occurred at ~490 Ma. This age is related to the orogen collapse (Pedrosa-Soares *et al.* 2011) and might also correspond to the age of amethyst crystallisation in hydrothermal veins at Felício dos Santos.

With respect to the solid inclusions of hematite present in amethyst from both hydrothermal vein and pegmatite environments, it is suggested that the mineralising fluid was Fe rich and thus possibly magmatic. According to Juchem (1999), goethite [FeO(OH)] is the most common solid inclusion in amethyst from Rio Grande do Sul, indicating that the fluid that resulted in amethyst crystallisation in volcanic rock cavities was also Fe rich. As is well known, amethyst colour is related to the presence of trivalent iron impurities within the crystal structure (e.g. Lehmann and Moore, 1966; Dennen and Puckett, 1972; Cohen

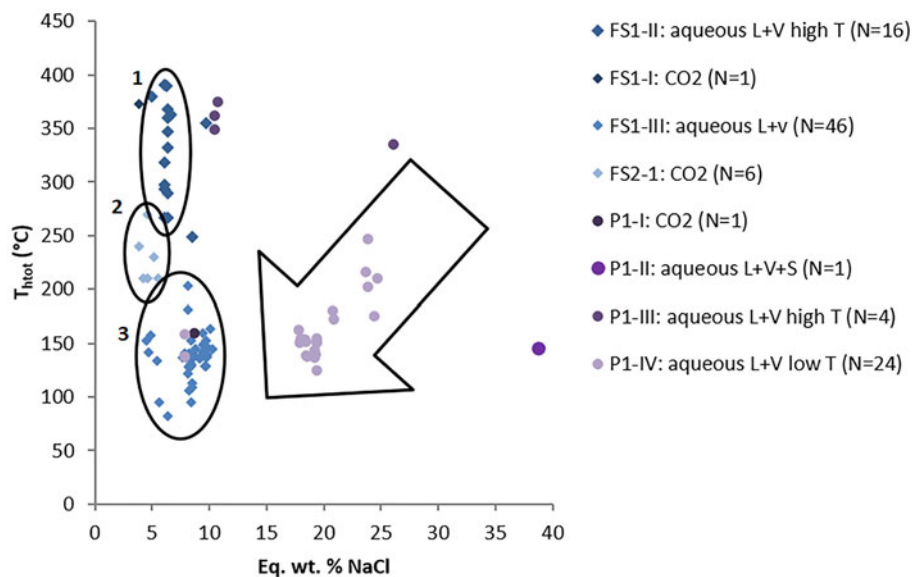


**Fig. 17.** Binary diagram of salinity versus homogenisation temperatures. FS1: Felício dos Santos hydrothermal vein – sample 1; FS2: Felício dos Santos hydrothermal vein – sample 2; P1: Pancas pegmatite sample. Ellipses delimitate FIAs of samples from the hydrothermal vein (Felício dos Santos); arrow delimitates most samples from the pegmatite (Pancas).

and Hassan, 1974; Cox, 1977; Cohen, 1985; Fischer *et al.*, 1999; Dedushenko *et al.*, 2004; Scholz *et al.*, 2012).

### Concluding remarks

Considering the geological environments investigated for amethyst growth, it can be concluded that pegmatite and hydrothermal deposits formed over a wide range of temperatures, from 82°C to 391°C, whereas amethyst from basalt cavities grew at lower temperatures, probably <100°C, according to previous studies (e.g. Juchem, 1999; Gilg *et al.* 2003; Commin-Fischer *et al.* 2010). High salinity values in fluid inclusions from the pegmatite sample correspond to the elevated salt content in residual fluids forming the pegmatites. Samples from hydrothermal veins show low-to-moderate salinity values ranging between 2.4 to 11.5 eq. wt.% NaCl. The presence of inclusions with H<sub>2</sub>O–CO<sub>2</sub>–NaCl composition in both hydrothermal vein and pegmatite samples suggests a metamorphic or magmatic source for the fluids. Hematite solid inclusions observed in amethyst from both hydrothermal vein and pegmatite environments indicate that the mineralising fluid was Fe rich and hence possibly magmatic.

**Acknowledgements.** This study was partially financed by the Coordenação de Aperfeiçoamento de Pessoal de Nível Superior – Brasil (CAPES) – Finance Code 001, by the concession of a grant during part of the first author's PhD studies at the Geology Department/UFMG. The authors are grateful to the Raman Spectroscopy Laboratory of the Metallurgy Department/Engineering School/UFMG, in the name of Professor Maria Sylvania Silva Dantas who carried out Raman analyses, and for the UFMG Microscopy Center, where thin sections were cut. We also thank the retired IG/USP physician Rosa Maria da Silveira Bello and the geologist Lucilia Aparecida Ramos de Oliveira for valuable comments on the manuscript.

### References

Almeida F.F.M. (1977) O cráton do São Francisco. *Revista Brasileira de Geociências*, **7**, 349–364.  
 Bodnar R.J. (2003) Introduction to fluid inclusions. Pp. 1–8 in: *Fluid Inclusions: Analysis and Interpretation* (I. Samson, A. Anderson A. and D. Marshall, editors). Mineralogical Association of Canada, Quebec.  
 Bodnar R.J. and Vityk M.O. (1994) Interpretation of microthermometric data for H<sub>2</sub>O–NaCl fluid inclusions. Pp. 117–130 in: *Fluid Inclusions in*

*Minerals: Methods and Applications* (B. de Vivo, M.L. Frezzotti, editors). Short Course IMA, Blacksburg, USA.  
 Bowers T.S. and Helgeson H.C. (1983) Calculation of the thermodynamic and geochemical consequences of nonideal mixing in the system H<sub>2</sub>O–CO<sub>2</sub>–NaCl on phase relations in geological systems: equation of state for H<sub>2</sub>O–CO<sub>2</sub>–NaCl fluids at high pressures and temperatures. *Geochimica et Cosmochimica Acta*, **47**, 1247–1275.  
 Brown P.E. and Hagemann S.G. (1995) MacFlinCor and its application to fluids in Archean lode–gold deposits. *Geochimica et Cosmochimica Acta*, **59**, 3943–3952.  
 Chaves M.L.S.C. and Coutinho D.C. (1992) Nota sobre a jazida de ametista da Fazenda Sobrado (Felício dos Santos – MG). *REM: Revista Escola de Minas*, **45**, 194–195.  
 Chaves M.L.S.C., Tolentino E.L.Jr., Dias C.H.D. and Romano A.W. (2017) Geologia, mineralogia, inclusões fluidas e gênese dos depósitos de titanita–epidoto de Capelinha, Minas Gerais. *Geologia USP Série Científica*, **17**, 3–18.  
 Cohen A.J. (1985) Amethyst color in quartz, the result of radiation protection involving iron. *American Mineralogist*, **70**, 1180–1185.  
 Cohen A.J. and Hassan F. (1974) Ferrous and ferric ions in synthetic alpha-quartz and natural amethyst. *American Mineralogist*, **59**, 719–728.  
 Commin-Fischer A., Berger G., Polvé M., Dubois M., Sardini P., Beaufort D. and Formoso M. (2010) Petrography and chemistry of SiO<sub>2</sub> filling phases in the amethyst geodes from the Serra Geral Formation deposit, Rio Grande do Sul, Brazil. *Journal of South American Earth Sciences*, **29**, 751–760.  
 Cox R.T. (1977) Optical absorption of the d4 ion Fe<sup>4+</sup> in pleochroic amethyst quartz. *Journal of Physics C Solid State Physics*, **10**, 4631.  
 Dardenne M.A. and Schobbenhaus C. (2003) Depósitos minerais no tempo geológico e épocas metalogénicas. Pp. 365–447 in: *Geologia, tectônica e recursos minerais do Brasil: texto, mapas e SIG* (L.A. Bizzi, C. Schobbenhaus, R.M. Vidotti and J.H. Gonçalves, editors). Companhia de Pesquisa de Recursos Minerais, Brasília.  
 Dedushenko S.K., Makhina I.B., Mar'in A.A., Mukhanov V.A. and Perfiliev Y.U.D. (2004) What oxidation state of iron determines the amethyst colour? *Hyperfine Interactions*, **156**, 417–422.  
 Dennen W.H. and Puckett A.M. (1972) On the chemistry and color of amethyst. *The Canadian Mineralogist*, **11**, 448–456.  
 Dias C.H., Chaves M.L.S.C., Juchem P.L. and Romano A.W. (2019) Ocorrências de ametista em basaltos do Triângulo Mineiro (Minas Gerais): comparações com depósitos similares do Rio Grande do Sul. *Pesquisas em Geociências*, **46**, e0822. doi:10.22456/1807-9806.97385  
 Dodd S.C., Macniocail C. and Muxworthy A.R. (2015) Long duration (>4Ma) and steady-state volcanic activity in the early Cretaceous Paraná-Etendeka Large Igneous Province: New paleomagnetic data from Namibia. *Earth and Planetary Science Letters*, **414**, 16–29.

- Dumanska-Slowik M, Tobola T, Jarmolowicz-Szulc K, Naglik B., Dylag J. and Szczerba J. (2017) Inclusion study of hourglass amethyst from Boudi (Morocco) by Raman microspectroscopy and microthermometric measurements. *Spectrochimica Acta Part A: Molecular and Biomolecular Spectroscopy*, **187**, 156–162.
- Fischer A.C., Krambrock K., Pinheiro M.V.B. and Juchem P.L. (1999) Natural and irradiated amethyst from Rio Grande do Sul studied by optical absorption and electron paramagnetic resonance. *Anais da Academia Brasileira de Ciências*, **71**, 823–824.
- Fogaça A.C.C. (2012) *Folha Diamantina, SE.23–Z–A–III, escala 1:100.000*. Convênio CODEMIGUFMG, Belo Horizonte.
- Frank H.T., Gomes M.E.B. and Formoso M.L.L. (2009) Revisão da extensão areal e do volume da formação Serra Geral, Bacia do Paraná, América do Sul. *Pesquisas em Geociências*, **36**, 49–57.
- Frezzotti M.L., Tecce F. and Casagli A. (2012) Raman spectroscopy for fluid inclusion analysis. *Journal of Geochemical Exploration*, **112**, 1–20.
- Gilg H.A. (2012) In the beginning: The origins of amethyst. Pp. 10–13 in: *Amethyst – Uncommon Vintage* (R. Balzer and H.A. Gilg, editors). Lithographie, Denver.
- Gilg H.A., Morteani G., Kostitsyn Y., Preinfalk C., Gatter I. and Strieder A.J. (2003) Genesis of amethyst geodes in basaltic rocks of the Serra Geral Formation (Ametista do Sul, Rio Grande do Sul, Brazil): a fluid inclusion, REE, oxygen, carbon, and Sr isotope study of basalt, quartz and calcite. *Mineralium Deposita*, **38**, 1009–1025.
- Goldstein R.H. and Reynolds T.J. (1994) *Systematics of Fluid Inclusions in Diagenetic Minerals*. Society for Sedimentary Geology Short Course 31, 199 pp.
- Juchem P.L. (1999) *Mineralogia, geologia e gênese dos depósitos de ametista da região do Alto Uruguai, Rio Grande do Sul*. PhD Thesis, Universidade de São Paulo, São Paulo, Brazil.
- Juchem P.L. (2013) O Distrito Mineiro de Ametista do Sul – roteiro de excursão. Pp. 7–15 in: *Seminário Brasileiro de Gemologia e Design de Joias*, 3.
- Juchem P.L., Hofmeister T., Brum T.M.M. (1990) Substâncias gemológicas no Rio Grande do Sul – modos de ocorrência e caracterização gemológica. Pp. 1436–1449 in: *Congresso Brasileiro de Geologia*, 36.
- Lehmann G. and Moore W.J. (1966) Color center in amethyst quartz. *Science*, **152**, 1061–1062.
- Leite C.A.S. et al. (2004). Folha SE.24-Rio Doce in: *Carta Geológica do Brasil ao Milionésimo* (C. Schobbenhaus, J.H. Gonçalves, J.O.S. Santos, M.B. Abram, R. Leão Neto, G.M.M. Matos, R.M. Vidotti, M.A.B. Ramos and J.D.A. de Jesus, editors). CPRM, Brasília.
- London D. (2008) *Pegmatites*. Mineralogical Association of Canada, Québec, 347 pp.
- London D. and Kontak D.J. (2012) Granitic pegmatites: scientific wonders and economic bonanzas. *Elements*, **8**, 257–261.
- Pedrosa-Soares A.C., Chaves M.L.S.C. and Scholz R. (2009) Field Trip Guide. Pp 1–28 in: *International Symposium on Granitic Pegmatites*. PEG2009, Belo Horizonte, Brazil, August 2009.
- Pedrosa-Soares A.C. et al. (2011) Late Neoproterozoic–Cambrian granitic magmatism in the Araçuaí orogen (Brazil), the Eastern Brazilian Pegmatite Province and related deposits. *Geological Society Special Publication*, **350**, 25–51.
- Piccirillo E.M. and Melfi A.J. (1988) *Mesozoic Flood Volcanism of the Paraná Basin: Petrogenetic and Geophysical Aspects*. IAG–USP, São Paulo, Brazil, 600 pp.
- Pinto C.P. and Silva M.A. (2014) *Mapa Geológico do Estado de Minas Gerais, escala 1:1.000.000*. Convênio CODEMIG/CPRM–SGB, Belo Horizonte, Brazil.
- Ramboz C., Pichavant M. and Weisbrod A. (1982) Fluid immiscibility in natural processes: Use and misuse of fluid inclusion data II. Interpretation of fluid inclusion data in terms of immiscibility. *Chemical Geology*, **37**, 29–48.
- Scholz R., Chaves M.L.S.C., Krambrock K., Pinheiro M.V.B., Barreto S.B. and Menezes M.G. (2012) Brazilian quartz deposits with special emphasis on gemstone quartz and its color treatment. Pp 139–159 in: *Quartz: Deposits, Mineralogy and Analytics* (J. Götze and R. Möckel, organisers). Springer–Verlag Berlin Heidelberg, New York.
- Shepherd T.J., Rankin A.H. and Alderton D.M. (1985) *A Practical Guide to Fluid Inclusion Studies*. Blackie, Glasgow, UK, 239 pp.
- Thiede D.S. and Vasconcelos P.M. (2010) Paraná flood basalts: Rapid extrusion hypothesis confirmed by new <sup>40</sup>Ar/<sup>39</sup>Ar results. *Geology*, **38**, 747–750.
- Tupinambá M., Baars F.J., Uhlein A., Grossi-Sad J.H. and Knauer L.G. (1996) *Folha Rio Vermelho, Mapa e Nota Explicativa*. Comig–UFMG, Belo Horizonte, Brazil.
- Tupinambá M., Baars F.J., Uhlein A., Grossi-Sad J.H. and Knauer L.G. (2012) *Folha Rio Vermelho, SE.23–Z–B–I, escala 1:100.000*. Convênio CODEMIGUFMG, Belo Horizonte, Brazil.
- Valente C.R., Lacerda Filho J.F., Rizzotto G.J., Lopes R.C., Romanini S.J., Oliveira I.W.B., Sachs L.L.B., Silva V.A. and Batista I.H. (2004) Folha SE.22-Goiânia in: *Carta Geológica Brasil ao Milionésimo* (C. Schobbenhaus, J.H. Gonçalves, J.O.S. Santos, M.B. Abram, R. Leão Neto, G.M.M. Matos, R.M. Vidotti, M.A.B. Ramos and J.D.A. de Jesus, editors). CPRM, Brasília.
- Vieira V.S., Silva M.A., Corrêa T.R. and Lopes NHB (2013) *Mapa geológico do Estado do Espírito Santo, escala 1:400.000*. CPRM, Belo Horizonte, Brazil.
- Yang K.H., Yun S.H. and Lee J.D. (2001) A fluid inclusion study of an amethyst deposit in the Cretaceous Kyongsang Basin, South Korea. *Mineralogical Magazine*, **65**, 477–487.
- Yardley B.W.D. (1983) Quartz veins and devolatilization during metamorphism. *Journal of the Geological Society of London*, **140**, 657–663.